

# Super-Resolution Generalized Eigenvalue Method with Truly Sub-Nyquist Sampling

Baoguo Liu, Huiguang Zhang, Wei Feng, Zongyao Liu, Zhen Zhang, Yanxu Liu

**Abstract**—The realization of spectral super-resolution sensing is of great significance in several applications, including radar, remote sensing, and wireless communication. However, in compressed spectrum sensing, spectrum leakage and the picket-fence effect pose considerable challenges for the accurate extraction of super-resolution signal components, while the hardware implementation of random sampling is another crucial factor that hinders the widespread application of compressed spectrum sensing. To address these problems, this study proposes a generalized eigenvalue method that exploits the incoherence between signal components and the linearity-preserving property of differential operations. The generalized eigenvalue method enables the accurate extraction of signal component parameters with super-resolution under sub-Nyquist sampling conditions. Furthermore, the proposed method is based on uniform sub-Nyquist sampling, which is truly sub-Nyquist sampling and effectively reduces the difficulty of hardware implementation. Moreover, unlike traditional compressed sensing techniques, the proposed method does not rely on the discrete Fourier transform framework, effectively eliminating spectral leakage and the picket-fence effect. Additionally, it greatly reduces the adverse effects of random sampling on signal reconstruction and hardware implementation.

**Index Terms**—compressed spectral sensing, generalized eigenvalue method, super-resolution extraction, truly sub-Nyquist sampling

## I. INTRODUCTION

### A. Overview of Compressed Spectrum Sensing Theory Series Methods

Ultra-wideband and high-throughput signals are becoming increasingly common in fields such as wireless communication [1], radar ranging [2], and computational imaging [3]. This trend poses unprecedented challenges in signal sampling, transmission, and processing. Compressed spectrum sensing (CSS), based on compressed sensing [4] and Fourier transform [5], effectively reduces the number of samples required to reconstruct a signal via frequency sparsity.

CSS provides a new solution to these problems and has consequently received widespread attention with in-depth research.

With the development of compressed sensing theory, scholars have proposed various implementations of CSS to adapt to different signal characteristics and application requirements. Mishali *et al.* proposed the modulated wideband converter (MWC) method and the "Xampling" method for sparse multiband signals and finite rate innovation signals to broaden the applicability of signal types. The MWC ensures signal recoverability by separating different band signals and performing random modulations [6]. This enables the MWC method to sample and reconstruct signals at frequencies much lower than the Nyquist rate, even when the carrier frequency is unknown [7], [8]. The "Xampling" method, based on joint subspace theory and the finite rate innovation property [9], effectively reduces the number of samples required for signal reconstruction by combining analog compression and nonlinear algorithms [10]. These two methods have recently been regarded as crucial breakthroughs in sub-Nyquist sampling theory [11]. However, with growing sub-bands and bandwidths, the system complexity and power consumption of MWC increase accordingly, posing challenges in practical application. To process large-scale signal sets, the sparse Fourier transform (SFT) proposed by Hassanieh *et al.* [12] provides an efficient CSS method that is suitable for the fast spectral analysis of large datasets, such as those at the terabyte level. SFT effectively reduces the number of samples required for extracting the main components by employing the barrel filter technique [13], [14]. However, the lack of a priori knowledge and the selection of bucket coefficients and filter parameters pose formidable challenges, primarily because inappropriate parameters can degrade the extraction accuracy.

Regarding computational cost, Romero *et al.* [15] introduced compressed covariance sensing (CCS) to address the processing requirements involved in reconstructing wideband analog signals. CCS involves developing a covariance matrix of the wideband signal from compressed samples, rather than directly reconstructing the signal itself [16]. The method efficiently minimizes the computational burden, which simplifies the process. However, while CCS simplifies computation, it imposes certain constraints. Unlike compressed sensing techniques that can precisely reconstruct the original signal, CCS may not achieve full signal reconstruction. Rauhut *et al.* [17] extensively studied structured random matrices for CSS, focusing specifically on the implementation of an observation matrix. These matrices possess a special structure that preserves their restricted

Manuscript received \*\*\*\* \*\*, 2024; revised \*\*\*\*\* \*\*, 2024 and \*\*\*\*\* \*\*, 2024; accepted \*\*\*\*\* \*\*, 2024. Date of publication \*\*\*\*\* \*\*, \*\*\*\*, date of current version February 10, 2025. This work was supported by National Natural Science Foundation of China (61571380, 61811530021, 61871341, U1632274, 61672335 and 61601276), Natural Science Foundation of Fujian Province of China (2018J06018 and 2016J05205), (*Corresponding author: BaoGuo Liu.*)

BaoGuo Liu, Huiguang Zhang, Wei Feng and Zongyao Liu are with Department of Mechanical and Electrical Engineering, Henan University of Technology, Zhengzhou, China (e-mail: [liubaoguo1979@sina.com](mailto:liubaoguo1979@sina.com)).

Zhen Zhang, Yanxu Liu is with the School of Mechanical Engineering, Zhengzhou University of Technology, Zhengzhou, China.

isometry property (RIP) [18]. Additionally, they streamline the implementation process and reduce the required storage [19], [20]. Structured random matrices provide a notable benefit over completely random Gaussian or Bernoulli matrices for practical applications. However, it is challenging to select a suitable structured random matrix that matches the unique properties of the signal and guarantees RIP. To achieve this, it is crucial to gain a thorough understanding of the characteristics of the signal and meticulously manage the construction of the matrix.

Eldar *et al.* made crucial advancements in hardware implementation. They developed a hardware system that can perform sub-Nyquist sampling and reconstruction of wideband signals via a MWC for the first time [6]. The study confirmed the practicality of the MWC technique and facilitated the integration of hardware into the Xampling framework [9], enabling the sampling and processing of signals within a subspace union. Pfetsch *et al.* presented a potential hardware implementation of an analog-to-information converter (AIC) [21]. The AIC performs sub-Nyquist sampling and reconstruction of analog signals by modulating the incoming analog signal using pseudo-random sequences [22] and then extracting the wideband signal by compressing the measurement matrix.

Note that the principal objective of this study is not to provide an exhaustive review of the field of compressed sensing. Our aim is to present a concise overview of the significant advances and central representative works in CSS theory, thereby enabling readers to quickly develop the requisite knowledge framework to comprehend the methodologies proposed in this study. Consequently, the literature review presented in this section may not encompass all aspects of CSS.

### B. Current Challenges in Compressed Sensing Spectral Methods

As previously stated, although remarkable progress has been made in CSS research based on standard compressed sensing theory, the impact of spectral leakage and the picket-fence effect on the accuracy of spectral sensing warrants further study. Additionally, the subsampling algorithm under the traditional uniform sampling condition, that is, truly sub-Nyquist sampling, rather than an algorithm based on random sampling, is also under-researched.

#### 1) **Non-Sparsification of Signals Caused by Discrete Fourier Transform (DFT) Spectral Leakage and Picket-Fence Effect:**

CSS generally leverages Fourier transform matrices and random matrix theory to derive an measurement matrix. However, the spectral leakage and picket-fence effect of the DFT may cause the signal to lose its original sparsity. Current research approaches this problem in two methods: by assuming that the signal is standard sparse, or by enforcing sparsity through hard thresholding. This undoubtedly affects the super-resolution extraction of the

frequency, amplitude, and phase of the reconstructed signal [23], [24].

#### 2) **Algorithms that Utilize Random Sampling Versus Truly Sub-Nyquist Sampling [25]:**

Currently, random sampling methods are extensively employed in compressed sensing to ensure the RIP of the sensing matrix. However, despite operating below the required sampling frequency of the Nyquist sampling theorem, random sampling poses two severe challenges. First, the computational complexity of reconstructing the signal after random sampling can be considered, and there remains a certain probability of failure, although it is relatively low. These limitations render compressed spectrum sensing primarily suitable for application scenarios with high sampling costs, relatively sufficient computational resources, and low real-time and resolution requirements [26], [27]. Second, the hardware implementation of random sampling presents a severe challenge, particularly to analog devices. This is because the majority of existing commercial devices are designed for uniform sampling, rather than random sampling. Furthermore, there is a paucity of studies on algorithms based on truly sub-Nyquist sampling with uniform sampling [28]-[30].

Solving the aforementioned problems is of immense practical importance for the viability of super-resolution extraction and hardware implementation. Currently, there is a critical need to investigate super-resolution algorithms that can overcome the restrictions of fast Fourier transform (FFT) in truly sub-Nyquist sampling.

### C. Main Achievements and Innovations

In CSS, spectral leakage and the picket-fence effect are key problems that affect super-resolution extraction, while difficulties in hardware implementation caused by random sampling have severely limited the application of CSS. To address these problems, we propose a novel method called the generalized eigenvalue method (GEM). GEM leverages the non-coherence and linear mapping relationship between signal components and their differential signals, along with a synchronized aliasing mechanism. GEM enables the super-resolution extraction of component frequencies, amplitudes, and phases of multi-frequency complex signals at truly sub-Nyquist sampling rates or even at arbitrary sampling rates. The key contributions of this paper are as follows:

#### 1) **Innovation in Theoretical Framework:**

GEM can be applied beyond the Fourier transform framework, which enhances precision in parameter extraction without being influenced by spectral leakage or the picket-fence effect. Moreover, GEM employs uniform sampling, which reduces the impact of random sampling noise and theoretically enables the extraction of signal components at frequencies below the Nyquist limit. Super-resolution can be achieved by sampling parameters at sub-Nyquist rates.

> REPLACE THIS LINE WITH YOUR MANUSCRIPT ID NUMBER (DOUBLE-CLICK HERE TO EDIT) <

## 2) Optimization of Sampling Length:

Unlike other CSS techniques, the sample length in the GEM method is determined solely by the inherent sparsity of the signal and is independent of the original length of the signal. This greatly reduces the size of the sampled data, enhancing the effectiveness of the algorithm and reducing system requirements.

## 3) Precise Extraction of Parameters of Linear Frequency-Modulation Signals:

This paper extends GEM to the multi-parameter eigenvalue problem (MEP) for the first time and successfully applies it to the extraction of parameters of linear frequency-modulation signals. This achievement enables blind and accurate parameter extraction at sub-Nyquist sampling rates.

## 4) Hardware Implementation Simplification:

GEM employs a low-speed, uniform sampling approach, which simplifies its practical implementation using commonly utilized circuit components. Consequently, the complexity and cost of the required hardware are reduced.

The GEM approach improves the precision of CSS considerably and simplifies hardware implementation. These findings offer innovative insights and solutions for signal processing, thereby improving CSS technology and leveraging its distinct advantages in real-world applications.

### D. Organization

The second section focuses on conducting a separate investigation and proving the generalized eigenvalue extraction theory for multi-frequency and linear frequency-modulation signals. The third section presents numerical test results to compare the performance of the GEM and the fast Fourier transform (FFT), evaluating the super-resolution spectrum sensing capability of the GEM under truly sub-Nyquist sampling with an ultra-wideband (UWB) signal. The fourth section elucidates the fundamental principles of sub-Nyquist sampling implementation of this algorithm and explores its potential for hardware implementation. These studies exemplify the innovative applications of GEM in signal processing and establish a theoretical foundation for future hardware implementation.

## II. PARAMETER EXTRACTION THEORY FOR MULTI-FREQUENCY COMPLEX SIGNALS AND LINEAR FREQUENCY-MODULATION BASED ON GENERALIZED EIGENVALUE METHOD

### A. Multi-frequency Signal Parameter Extraction Theory

**Definition 1.** A multi-frequency complex signal  $x(t)$  is defined as follows:

$$x(t) = \sum_{i=1}^m a_i e^{j(2\pi f_i t + \varphi_{i0})}. \quad (1)$$

where  $f_i$ ,  $a_i$ , and  $\varphi_{i0}$  denote the frequency, amplitude, and initial phase of the  $i$ -th component, and  $m$  indicates the number of components.

The first-order derivative of  $x(t)$  is denoted as  $\dot{x}(t)$ . The Hankel matrix discretized and constructed for  $x(t)$  is  $X$ , and that discretized and constructed for  $\dot{x}(t)$  is  $D_x$ , where

$$X = \begin{pmatrix} x_1 & x_2 & \cdots & x_n \\ x_2 & x_3 & \cdots & x_{n+1} \\ \vdots & \vdots & \ddots & \vdots \\ x_n & x_{n+1} & \cdots & x_{2n-1} \end{pmatrix}, D_x = \begin{pmatrix} \dot{x}_1 & \dot{x}_2 & \cdots & \dot{x}_2 \\ \dot{x}_2 & \dot{x}_3 & \cdots & \dot{x}_{n+1} \\ \vdots & \vdots & \ddots & \vdots \\ \dot{x}_n & \dot{x}_{n+1} & \cdots & \dot{x}_{2n-1} \end{pmatrix}. \quad (2)$$

Construct the generalized eigenvalue equation of  $X$  to  $D_x$ :

$$D_x u = \lambda X u, \quad (3)$$

where  $\lambda$ ,  $u$  are the generalized eigenvalues and generalized eigenvectors of  $D_x$  to  $X$ .

**Proposition 1.** When  $n \geq m$ , the generalized eigenvalue equation, expressed as (3), for the multi-frequency complex signal yields  $m$  non-zero complex generalized eigenvalues  $\lambda_i$ , given by the following equations:

$$\lambda_i = j2\pi f_i. \quad (4)$$

**Proof.** For simplicity, (2.1) is simplified to the following form:

$$x(t) = \sum_{i=1}^m a_i e^{j(\omega_i t + \varphi_{i0})} \quad (5)$$

The first derivative of  $x(t)$  is:

$$\dot{x}(t) = \sum_{i=1}^m j \omega_i a_i e^{j(\omega_i t + \varphi_{i0})}. \quad (6)$$

For the sake of simplicity, the following provisions are made:

$$s_i = e^{j\omega_i \Delta t}, \alpha_i = a_i e^{j\varphi_{i0}} \quad (7)$$

By employing the definitions of  $X, D_x$ , and (2), (3), and (6), (7), we derive the following results:

$$X = \begin{pmatrix} \sum_{i=1}^m \alpha_i s_i & \sum_{i=1}^m \alpha_i s_i^2 & \cdots & \sum_{i=1}^m \alpha_i s_i^n \\ \sum_{i=1}^m \alpha_i s_i^2 & \sum_{i=1}^m \alpha_i s_i^3 & \cdots & \sum_{i=1}^m \alpha_i s_i^{n+1} \\ \vdots & \vdots & \ddots & \vdots \\ \sum_{i=1}^m \alpha_i s_i^n & \sum_{i=1}^m \alpha_i s_i^{n+1} & \cdots & \sum_{i=1}^m \alpha_i s_i^{2n-1} \end{pmatrix}$$

$$D_x = \begin{pmatrix} \sum_{i=1}^m j \omega_i \alpha_i s_i & \sum_{i=1}^m j \omega_i \alpha_i s_i^2 & \cdots & \sum_{i=1}^m j \omega_i \alpha_i s_i^n \\ \sum_{i=1}^m j \omega_i \alpha_i s_i^2 & \sum_{i=1}^m j \omega_i \alpha_i s_i^3 & \cdots & \sum_{i=1}^m j \omega_i \alpha_i s_i^{n+1} \\ \vdots & \vdots & \ddots & \vdots \\ \sum_{i=1}^m j \omega_i \alpha_i s_i^n & \sum_{i=1}^m j \omega_i \alpha_i s_i^{n+1} & \cdots & \sum_{i=1}^m j \omega_i \alpha_i s_i^{2n-1} \end{pmatrix}. \quad (8)$$

Subsequently, we investigate the diagonalization of  $X, D_x$  with Vandermonde decomposition [31], [32]. For Hankel matrices  $X_i$  on the components of  $x(t)$ ,

$$X_i = \begin{pmatrix} \alpha_i s_i & \alpha_i s_i^2 & \cdots & \alpha_i s_i^n \\ \alpha_i s_i^2 & \alpha_i s_i^3 & \cdots & \alpha_i s_i^{n+1} \\ \vdots & \vdots & \ddots & \vdots \\ \alpha_i s_i^n & \alpha_i s_i^{n+1} & \cdots & \alpha_i s_i^{2n-1} \end{pmatrix} \quad (9)$$

$$= (1, s_i, \dots, s_i^{n-1})^T \alpha_i s_i (1, s_i, \dots, s_i^{n-1})$$

where

$$S_{ci} = (1 \quad s_i \quad \cdots \quad s_i^{n-1}). \quad (10)$$

The matrix  $X$  can be represented as follows:

> REPLACE THIS LINE WITH YOUR MANUSCRIPT ID NUMBER (DOUBLE-CLICK HERE TO EDIT) <

$$\begin{aligned}
 X &= \sum_{i=1}^m X_i \\
 &= \sum_{i=1}^m S_{ci}^T \begin{pmatrix} \alpha_1 s_1 & & & \\ & \alpha_2 s_2 & & \\ & & \ddots & \\ & & & \alpha_m s_m \end{pmatrix} S_{ci} \\
 &= S_c^T \begin{pmatrix} \alpha_1 s_1 & & & \\ & \alpha_2 s_2 & & \\ & & \ddots & \\ & & & \alpha_m s_m \end{pmatrix} S_c
 \end{aligned} \quad (11)$$

and

$$S_c = [S_{c1}^T, S_{c2}^T, \dots, S_{cm}^T]^T, \quad (12)$$

where  $S_c$  represents the Vandermonde matrix of the Hankel matrix  $X$  formed by the discrete multiple-frequency complex signal.

Performing a Vandermonde decomposition of the Hankel matrix  $D_{x_i}$  with discrete components  $\dot{x}(t)$ :

Thus, from (10) and (12),  $D_x$  can be expressed as follows:

$$D_x = \sum_{i=1}^m D_{x_i} \quad (13)$$

$$= S_c^T \begin{pmatrix} j\omega_1 \alpha_1 s_1 & & & \\ & j\omega_2 \alpha_2 s_2 & & \\ & & \ddots & \\ & & & j\omega_m \alpha_m s_m \end{pmatrix} S_c$$

Substituting (11) and (13) into (3) yields:

$$= S_c^T \begin{pmatrix} (\lambda - j\omega_1 \alpha_1) s_1 & & & \\ & (\lambda - j\omega_2) \alpha_2 s_2 & & \\ & & \ddots & \\ & & & (\lambda - j\omega_m) \alpha_m s_m \end{pmatrix} S_c u \quad (14)$$

Equation (14) shows that the rank of  $D_x - \lambda X$  decreases from  $m$  to  $m-1$  only when  $\lambda = j\omega_i$ . This implies the existence of a vector  $v$  corresponding to  $j\omega_i$ , which satisfies the condition for a non-zero solution to  $(D_x - \lambda X)u = 0$ . According to the definition of generalized eigenvalues,  $j\omega_i$  represents the generalized eigenvalue of (3). Therefore, the proof of

Proposition 1 is complete. Although the aforementioned proof is based on multi-frequency complex signals, it is straightforward to extend the application of this method to real multi-frequency signals via Euler's formula. A more intuitive understanding of GEM can be gained by Fig. 1.

The mechanism of the GEM can be explained as shown in Fig. 1:

- At first, as illustrated in the above figure, the signal designated as  $x(t)$  is the one to be decomposed. The dark blue curve represents the original signal, and the sinusoidal curves of varying colors represent the individual signal components. The signal  $x(t)$  is then differentiated in the time domain to obtain the difference signal  $\dot{x}(t)$ . Based on the properties of the differential operation, the frequencies of the differential signal  $\dot{x}(t)$  and the components of the original signal  $x(t)$  remain consistent.
- Subsequently, as illustrated in the upper portion of the middle section, following the sampling or discretization of  $x(t)$ , the corresponding Hankel matrix  $X$  is constructed. The matrices of varying colors represent distinct components. The Hankel matrix  $D_x$ , constructed from the difference signal  $\dot{x}(t)$ , is shown in the lower portion of the middle section.
- Finally, as illustrated in the figure on the right, the Hankel matrix on both sides of the generalized eigenvalue equation is decomposed using Vandermonde decomposition. Subsequently, the corresponding terms are combined to transform the generalized eigenvalue equation into the product of a Vandermonde matrix and a diagonal matrix. The Vandermonde matrix is represented by  $S$ , and its transpose is denoted by  $S^T$ .  $D$  represents a diagonal matrix that contains the generalized eigenvalues and the angular frequency information of the components.

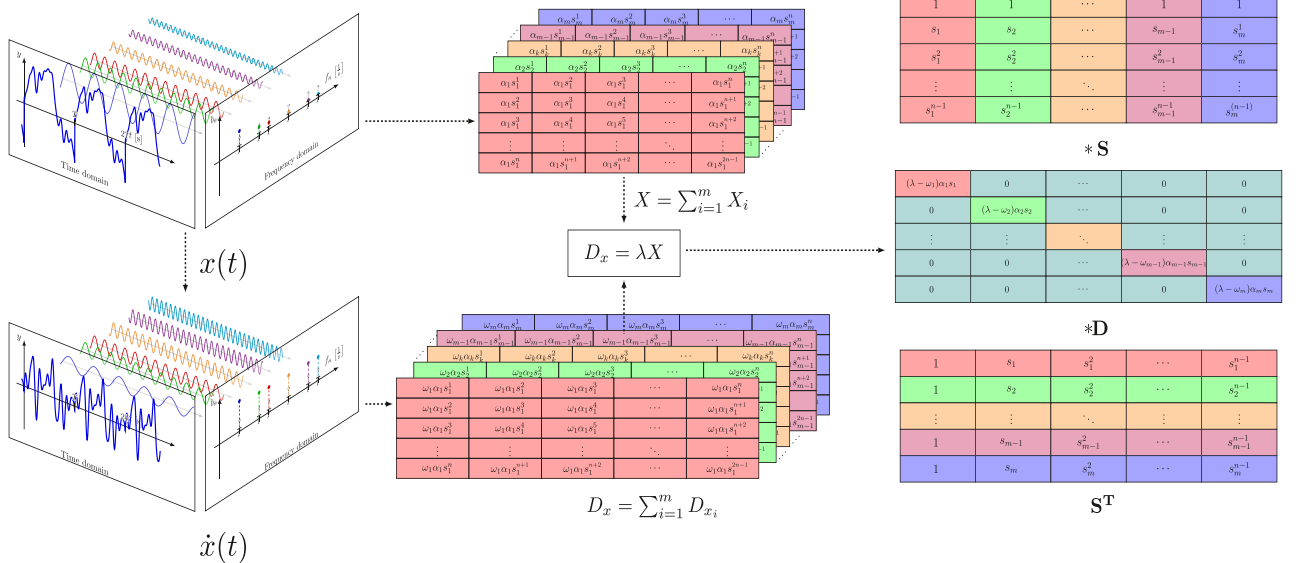


**Fig. 1** Mechanism of GEM, mechanism of the generalized eigenvalue method, and the meanings and explanations of each part are detailed in the main section.

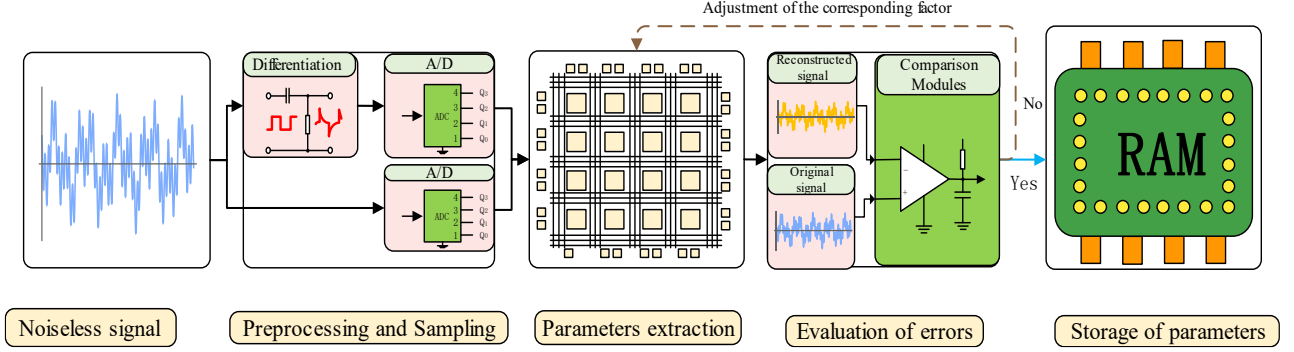


**Fig. 2** Flowchart of the hardware implementation of the generalized eigenvalue method, as demonstrated in the figure, our proposed method requires the differentiation of the signal to be performed in the analog domain.

The process flow of GEM is summarized below:

First, the original signal  $x(t)$  is differentiated by an analog differential device to obtain the differential signal  $\dot{x}(t)$ . The original signal  $x(t)$  and the differential signal  $\dot{x}(t)$  are synchronously sampled at the same sampling rate (either satisfying or not satisfying the Nyquist sampling rate). According to these discretized signals, the corresponding Hankel matrices  $X$  and  $D_x$  are constructed. Subsequently, the generalized eigenvalue equations in (3) are constructed according to  $X$  and  $D_x$ . Finally, the parameters are obtained by solving (3). The following flowchart in Fig. 2 shows the implementation flow of our proposed method.

### 1) Theory of Component Magnitude And Phase Extraction For Multi-Frequency Complex Signals

**Definition 2.** A multi-frequency complex signal  $g(t)$  is defined as follows:

$$g(t) = \sum_{i=1}^m e^{j2\pi f_i t} \quad (15)$$

The Hankel matrix  $G$  is formed from the discretized  $g(t)$ .

$$G = \begin{pmatrix} g_1 & g_2 & \cdots & g_n \\ g_2 & g_3 & \cdots & g_{n+1} \\ \vdots & \vdots & \ddots & \vdots \\ g_n & g_{n+1} & \cdots & g_{2n-1} \end{pmatrix}, \quad (16)$$

The Hankel matrix constructed from the discrete components of  $g(t)$  is denoted as  $G$ .

**Corollary 1.** Once the frequencies of the components are determined via Proposition 1, the amplitude and phase of the multi-frequency signal are obtained using (17) [33], [34].

$$a_i e^{j\varphi_{i0}} = \frac{u_i^H X u_i}{u_i^H G_i u_i} \quad (17)$$

**Proof.** For simplicity, (15) can be expressed as follows:

$$g(t) = \sum_{i=1}^m e^{j\omega_i t} \quad (18)$$

Thus, from (10) and (15), the constructed Hankel matrix  $G$  with a discrete  $g(t)$  is as follows:

$$G = \begin{pmatrix} \sum_{i=1}^m s_i & \sum_{i=1}^m s_i^2 & \cdots & \sum_{i=1}^m s_i^n \\ \sum_{i=1}^m s_i^2 & \sum_{i=1}^m s_i^3 & \cdots & \sum_{i=1}^m s_i^{n+1} \\ \vdots & \vdots & \ddots & \vdots \\ \sum_{i=1}^m s_i^n & \sum_{i=1}^m s_i^{n+1} & \cdots & \sum_{i=1}^m s_i^{2n-1} \end{pmatrix} \quad (19)$$

For all components  $G_i$  of  $G$ , it holds that:

$$G_i = \begin{pmatrix} s_i & s_i^2 & \cdots & s_i^n \\ s_i^2 & s_i^3 & \cdots & s_i^{n+1} \\ \vdots & \vdots & \ddots & \vdots \\ s_i^n & s_i^{n+1} & \cdots & s_i^{2n-1} \end{pmatrix} \quad (20)$$

Thus, from (3), (9), and (20), it follows that

$$u_i^H X_i u_i = a_i e^{j\varphi_{i0}} u_i^H G_i u_i \quad (21)$$

For the  $i$ -th generalized eigenvector  $u_i$ ,  $u_i^H X_i u_i$  can be substituted by  $u_i^H X u_i$ , given that the generalized eigenvector are orthogonally weighted  $u_i^H X u_i = 0 (i \neq k)$ . Thus, (21) can be expressed in the form of (17), thereby proving Corollary 1.

### B. Theory of Linear Frequency-Modulation Signal Parameter Extraction

#### 1) Theory for Extracting Initial Frequency and Frequency-Modulation Index of Linear Frequency-Modulated Signal

**Definition 3.** Consider a linear frequency-modulated signal denoted by  $y(t)$ , which has the following form:

$$y(t) = a e^{j(kt^2 + 2\pi f t + \varphi_0)} \quad (22)$$

where  $k, f, a, \varphi_0$  represent the corresponding modulation index, initial frequency, amplitude, and initial phase, respectively.

The first derivative of  $y(t)$  is  $\dot{y}(t)$ . The Hankel matrices constructed from the discretized  $y(t)$  and  $\dot{y}(t)$  are denoted by  $Y, \dot{Y}$  respectively, where

$$Y = \begin{pmatrix} y_1 & y_2 & \cdots & y_n \\ y_2 & y_3 & \cdots & y_{n+1} \\ \vdots & \vdots & \ddots & \vdots \\ y_n & y_{n+1} & \cdots & y_{2n-1} \end{pmatrix}, \dot{Y} = \begin{pmatrix} \dot{y}_1 & \dot{y}_2 & \cdots & \dot{y}_n \\ \dot{y}_2 & \dot{y}_3 & \cdots & \dot{y}_{n+1} \\ \vdots & \vdots & \ddots & \vdots \\ \dot{y}_n & \dot{y}_{n+1} & \cdots & \dot{y}_{2n-1} \end{pmatrix}, \quad (23)$$

Define  $Y_H$  as follows:

> REPLACE THIS LINE WITH YOUR MANUSCRIPT ID NUMBER (DOUBLE-CLICK HERE TO EDIT) <

$$Y_H = \begin{pmatrix} t_1 y_1 & t_2 y_2 & \cdots & t_n y_n \\ t_2 y_2 & t_3 y_3 & \cdots & t_{n+1} y_{n+1} \\ \vdots & \vdots & \ddots & \vdots \\ t_n y_n & t_{n+1} y_{n+1} & \cdots & t_{2n-1} y_{2n-1} \end{pmatrix}, \quad (24)$$

where  $t_i$  is the temporal value that corresponds to element  $y_i$  in  $Y$ .

Form (25) as follows [35], [36]:

$$\dot{Y}v - (\lambda_L Y_H + \mu_L Y)v = 0 \quad (25)$$

**Proposition 2.** The solution to the multi-parameter eigenvalue system (25) for linear frequency-modulated signals contains  $n$  repeated eigenvalues  $(\lambda, \mu)$ , given by the following equation:

$$(\lambda_L, \mu_L) = (j2k, j2\pi f) \quad (26)$$

**Proof.** It follows from (22) that

$$\dot{y}(t) = j(2kt + 2\pi f)ae^{j(kt^2 + 2\pi ft + \varphi_0)} \quad (27)$$

For simplicity, let  $\omega = 2\pi f$ , then by the definition of  $y$  and (27):

$$\begin{aligned} \dot{Y} &= \begin{pmatrix} \dot{y}_1 & \dot{y}_2 & \cdots & \dot{y}_n \\ \dot{y}_2 & \dot{y}_3 & \cdots & \dot{y}_{n+1} \\ \vdots & \vdots & \ddots & \vdots \\ \dot{y}_n & \dot{y}_{n+1} & \cdots & \dot{y}_{2n-1} \end{pmatrix} \\ &= j \begin{pmatrix} (2kt_1 + \omega)y_1 & (2kt_2 + \omega)y_2 & \cdots & (2kt_n + \omega)y_n \\ (2kt_2 + \omega)y_2 & (2kt_3 + \omega)y_3 & \cdots & (2kt_{n+1} + \omega)y_{n+1} \\ \vdots & \vdots & \ddots & \vdots \\ (2kt_n + \omega)y_n & (2kt_{n+1} + \omega)y_{n+1} & \cdots & (2kt_{2n-1} + \omega)y_{2n-1} \end{pmatrix} \\ &= j2kY_H + j\omega Y. \end{aligned} \quad (28)$$

We perform right-joint SVD on matrices  $Y$  and  $Y_H$  [37], [38], which yields

$$Y = U_y D_y V_{yH}, Y_H = U_H D_H V_{yH}. \quad (29)$$

Here, the left singular vector matrices for  $y$  and  $y_H$  in the right-joint SVD are denoted as  $U_y$  and  $U_H$ , respectively. The associated singular vectors are represented as  $(u_y)_i, (u_H)_i$ . Diagonal matrices  $D_y, D_H$  represent the diagonal elements in the right-joint SVD. The diagonal elements are denoted as  $(d_y)_i, (d_H)_i$ . Matrix  $V_{yH}$  represents the right singular vectors that are common in the right-joint SVD.

Substituting (28) and (29) into (25) yields

$$\begin{aligned} &\dot{Y}u - (\lambda_L Y_H + \mu_L Y)u \\ &= (j2kY_H + j\omega Y)u - (\lambda_L Y_H + \mu_L Y)u \\ &= ((j2k - \lambda_L)U_y D_y - (j\omega - \mu_L)U_H D_H)V_{yH}u \\ &= \begin{bmatrix} (j2k - \lambda_L)(u_y)_1 (d_y)_1 - (j\omega - \mu_L)(u_H)_1 (d_H)_1 \\ \vdots \\ (j2k - \lambda_L)(u_y)_i (d_y)_i - (j\omega - \mu_L)(u_H)_i (d_H)_i \\ \vdots \\ (j2k - \lambda_L)(u_y)_n (d_y)_n - (j\omega - \mu_L)(u_H)_n (d_H)_n \end{bmatrix} V_{yH}u \end{aligned} \quad (30)$$

Then if and only if  $(\lambda_L, \mu_L) = (j2k, j2\pi f)$  :

$$(j2k - \lambda_L)(u_y)_i (d_y)_i - (j\omega - \mu_L)(u_H)_i (d_H)_i = 0 \quad (31)$$

Therefore, if  $(\lambda_L, \mu_L) = (j2k, j2\pi f)$ , there exists a non-zero solution  $u$  to the null space of (30). This indicates the existence of a non-zero eigenvector  $u$  that corresponds to the

eigenvalue  $(j2k, j2\pi f)$  that satisfies (25). Hence, to multi-parameter eigenvalue theory, it can be inferred that  $(j2k, j2\pi f)$  denotes the two-parameter eigenvalue pair of (25). Thus, the demonstration of Proposition 2 is complete. To determine the solution for  $(\lambda_L, \mu_L)$ , one can construct another two-parameter eigenvalue equation with a similar form to (25) and create a system of equations with (25). The solution of this system can then be obtained utilizing the theory of multi-parameter eigenvalues.

## 2) Theory of Extracting Component Amplitude and Phase from Linear Frequency-Modulated Signals

**Definition 4.** Let a linear frequency-modulated signal be denoted as  $l(t)$ , with the following form:

$$l(t) = e^{j(kt^2 + 2\pi ft)}, \quad (32)$$

where  $k$  and  $f$  denote the corresponding frequency-modulation index and start frequency, respectively.

The Hankel matrix constructed from discretized  $l(t)$  is denoted as  $L$ , where

$$L = \begin{pmatrix} l_1 & l_2 & \cdots & l_n \\ l_2 & l_3 & \cdots & l_{n+1} \\ \vdots & \vdots & \ddots & \vdots \\ l_n & l_{n+1} & \cdots & l_{2n-1} \end{pmatrix} \quad (33)$$

Construct a generalized eigenvalue equation in the form of (3):

$$Yv = \lambda_{Ap}Lv \quad (34)$$

**Corollary 2.** Once the start frequency and frequency-modulation index of the chirp signal are determined via Proposition 2, the amplitude and initial phase can be calculated using (35).

$$\lambda_{Ap} = ae^{j\varphi_0} \quad (35)$$

**Proof.** From the definitions of  $Y$  and  $L$ , and using (22) and (30), it can be concluded that

$$y_i = ae^{j\varphi_0}l_i \quad (36)$$

Then, for  $Y$  and  $L$ , each row  $y_{C_{0i}}$  and  $l_{C_{0i}}$  has the following relationship:

$$\begin{bmatrix} (\lambda_{Ap} - ae^{j\varphi_0})l_1 \\ \vdots \\ (\lambda_{Ap} - ae^{j\varphi_0})l_i \\ \vdots \\ (\lambda_{Ap} - ae^{j\varphi_0})l_n \end{bmatrix} v = 0 \quad (37)$$

That is, when  $\lambda_{Ap} = ae^{j\varphi_0}$ , there exists a non-zero vector that satisfies  $Yv = \lambda_{Ap}Lv$ . According to generalized eigenvalue theory,  $ae^{j\varphi_0}$  is the generalized eigenvalue of  $Yv = \lambda_{Ap}Lv$ . Moreover, the magnitude and phase angle of the generalized eigenvalue  $\lambda_{Ap}$  correspond to the amplitude  $a$  and initial phase  $\varphi_0$  of the linear frequency-modulated signal, respectively, thus proving Corollary 2.

> REPLACE THIS LINE WITH YOUR MANUSCRIPT ID NUMBER (DOUBLE-CLICK HERE TO EDIT) <

### C. Algorithm Implementation

#### 1. GEM signal processing algorithm:

---

##### Algorithm 1: GEM signal processing algorithm

---

**Input:** Multi-frequency time-domain signal

**Output:** The frequency, amplitude, and initial phase of the components

- 1: Sampling the processed multi-frequency time-domain signal and its derivative signal.
- 2: Construct a generalized eigenvalue equation of the form  $D_x u = \lambda X u$  based on the theories discussed in Section II.A to calculate the frequencies of the components
- 3: Calculate the frequency amplitudes and initial phases of the components according to the theories discussed in Section II.A

---

#### 2. GEM signal processing algorithm:

---

##### Algorithm 2: GEM signal processing algorithm:

---

**Input:** Linear frequency-modulation time-domain signal.

**Output:** Start frequency, FM parameters, amplitude, initial phase.

- 1: Preprocess the linear frequency-modulated (LFM) time-domain signal by filtering and noise reduction.
- 2: Sample the processed LFM signal and its analog derivative signal within the time interval  $T_1$ .
- 3: Similar to Step 2, but sampling is required over another time interval  $T_2$ .
- 4: Referring to the theories discussed in Section 2.2, construct a system of equations formed by equations like  $\dot{Y}v - (\lambda_L Y_H + \mu_L Y)v = 0$
- 5: Based on the theory of multi-parameter eigenvalues, solve the system of equations constructed in Step 4 to determine the starting frequency and frequency-modulation parameters.
- 6: Refer to Section II.B for the theory and solve the linear frequency-modulation amplitude and initial phase based on step 5.

---

### III. ALGORITHM VALIDATION

In the second section, we thoroughly explored and rigorously proved the theoretical foundation of the proposed algorithm for exactly extracting parameters under arbitrary sampling frequencies. Subsequent sections systematically investigate the performance of the algorithm by examining its statistical properties and evaluating its effectiveness in practical applications. The subsequent sections of this study are organized as follows:

First, under noise-free conditions, the parameter results

extracted using the proposed algorithm are compared with those obtained using the fast Fourier transform (FFT) method with extra-long samples at various sampling frequencies. This comparison aims to demonstrate the advantages of the proposed algorithm in terms of accurate parameter extraction.

In the application research section, we first comprehensively compare the performance of the GEM method with CSS and SFT in UWB spectrum sensing. This comparison highlights the advantages of the GEM method for spectrum sensing tasks. Subsequently, we explore the application of the MEM algorithm in processing raw GNSS Doppler signals from a high-speed aircraft to extract velocity and acceleration information. This study demonstrates the effectiveness and adaptability of the algorithm in addressing challenging dynamic signal extraction problems. Additionally, we aim to verify the theoretical accuracy of the proposed algorithm and showcase its potential for real-world applications, providing valuable insights and tools for researchers and practitioners in the signal processing field.

#### A. Comparative Analysis of GEM and FFT Extraction Accuracy under Noise-Free Conditions

In the absence of noise, we compared the accuracy of the parameters extracted using the proposed algorithm and the FFT method at various sampling frequencies. The number of components of the signal is  $m = 10$ , and the true frequency  $f$ , amplitude  $A$ , and phase are presented in Table I. The sampling frequencies are 2.5 times for FFT and approximately 0.01 times the maximum component frequency for GEM. The GEM sample length is 38, which is  $4m-2$  of the original signal and the differential signal according to Proposition 1. It is well known that spectral leakage and the picket fence effect degrade the spectral resolution of FFT. To address this problem, scholars have proposed various improvement methods, such as the interpolated Fourier transform and zoom-FFT. The interpolated Fourier transform enhances the frequency analysis accuracy by performing interpolation operations at the main lobe peak of the spectrum and its adjacent points. Zoom-FFT, on the other hand, improves the analysis accuracy by refining the local frequency domain of the signal. However, both methods inherently require a longer equivalent signal sampling length. Therefore, we adopted an equivalent method, which involves using signals longer than the GEM to compare the spectral resolutions of the two methods. The FFT sample length is 1024. The results are presented in Table II, Fig. 3, and Fig. 4.

TABLE I  
THEORETICAL REFERENCE VALUES FOR MULTI-FREQUENCY  
SIGNAL COMPONENT PARAMETERS

N	1	2	3	4	5	6	7	8	9	10
$f(\text{Hz})$	935	957	1297	1317.5	3120	3135	4460	5530	5970	7990
A	1.5	3.5	2	0.1	1.2	0.8	2.5	0.8	1	0.3
$\Phi_i$ (°)	30	50	170	230	90	145	360	330	280	360

TABLE II  
COMPARISON OF FFT AND GEM FOR MULTI-FREQUENCY SIGNAL COMPONENT PARAMETERS

N	Relative error of FFT			Relative error of GEM methods with Nyquist sampling			Relative error of GEM methods with truly Sub-Nyquist sampling		
	$\Delta f_i$	$\Delta A_i$	$\Delta \Phi_i$	$\Delta f_i$	$\Delta A_i$	$\Delta \Phi_i$	$\Delta f_i$	$\Delta A_i$	$\Delta \Phi_i$
1	*	*	*	0	-7.3E-14	7.53E-13	0	-7.3E-14	7.53E-13
2	1.04E-02	8.03E-02	5.00E-01	0	5.32E-14	-3.1E-13	0	5.32E-14	-3.1E-13
3	1.58E-02	3.08E-01	9.06E-01	1.75E-16	-7.1E-13	-1.6E-13	1.75E-16	-7.1E-13	-1.6E-13
4	*	*	*	5.18E-16	-6.4E-12	1.79E-12	5.18E-16	-6.4E-12	1.79E-12
5	4.45E-03	1.91E-01	6.83E-01	0	-7E-14	6.88E-14	0	-7E-14	6.92E-14
6	*	*	*	0	-3.1E-14	2.09E-13	0	-3.1E-14	2.09E-13
7	6.11E-03	3.32E-02	1.70E-01	0	3.94E-13	-2.7E-14	0	3.94E-13	-2.7E-14
8	1.07E-02	1.52E-03	3.36E-01	1.64E-16	-1.5E-14	1.35E-13	1.64E-16	-1.5E-14	1.35E-13
9	1.54E-02	3.39E-01	6.30E-01	0	5.98E-11	-3.3E-11	0	5.98E-11	-3.3E-11
10	4.99E-03	2.92E-01	3.95E-02	-1.1E-16	-3.8E-12	9.67E-13	-1.1E-16	-3.8E-12	9.66E-13

$x_1, x_4,$  and  $x_6$  marked with an "\*" indicate that the FFT method failed to extract those components even at extra-long samples.

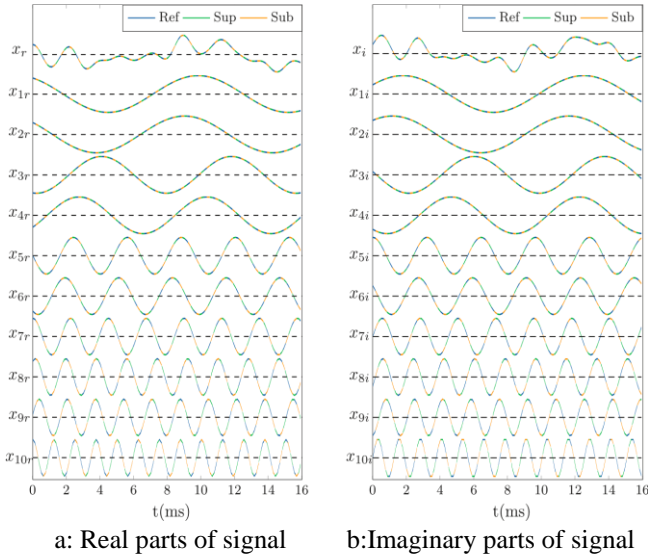
Table II presents the relative errors of the GEM and FFT methods for extracting the component frequencies, amplitudes, and phases at different sampling frequencies. Specifically, components  $x_1, x_4,$  and  $x_6$  marked with an "\*" indicates that the FFT method failed to extract them.

Table II reveals that the largest errors primarily originate from adjacent signal components with the smallest frequency intervals and the greatest amplitude differences. These errors are attributed to both the algorithm and inherent limitations in numerical calculations performed by computers. By contrast, the errors for other components in the table are significantly smaller. Evidently, the proposed GEM method can provide more accurate results than the FFT method when extracting the frequency, amplitude, and phase of signal components, even under sub-Nyquist sampling.

Fig. 3 presents a comparison between the component signals reconstructed from the parameters extracted by the GEM and the theoretical values. The legend "Ref" represents the theoretical values, while "Sup" and "Sub" correspond, respectively, to reconstruction results that satisfy the Nyquist sampling theorem and sub-Nyquist sampling conditions.

In Fig. 3,  $x_r$  and  $x_i$  represent the real and imaginary parts of the signal  $x(t)$ , respectively, whereas  $x_{1r}$  to  $x_{10r}$  denote the real parts of components 1 through 10, where  $x_{1i}$  to  $x_{10i}$  are their corresponding imaginary parts. It is evident from the figure that the computational results of the GEM are highly consistent with the theoretical values, regardless of whether the Nyquist sampling theorem is satisfied. This result visually confirms the accuracy and reliability of the GEM at various sampling frequencies, further validating its effectiveness for parameter extraction.

Fig. 4 illustrates the distinctions in parameter extraction between FFT and GEM in the frequency domain. This



a: Real parts of signal      b: Imaginary parts of signal  
**Fig. 3** Multi-frequency complex signals and their component signals, where  $x_r$  and  $x_i$  correspond to the time-domain signals of the real and imaginary parts of the original signal, respectively, and below them are the time-domain signals of the real and imaginary parts of each component.



> REPLACE THIS LINE WITH YOUR MANUSCRIPT ID NUMBER (DOUBLE-CLICK HERE TO EDIT) <

comparison supports the earlier conclusion that, irrespective of whether the Nyquist sampling theorem is satisfied, the GEM method consistently aligns with the theoretical parameter values.

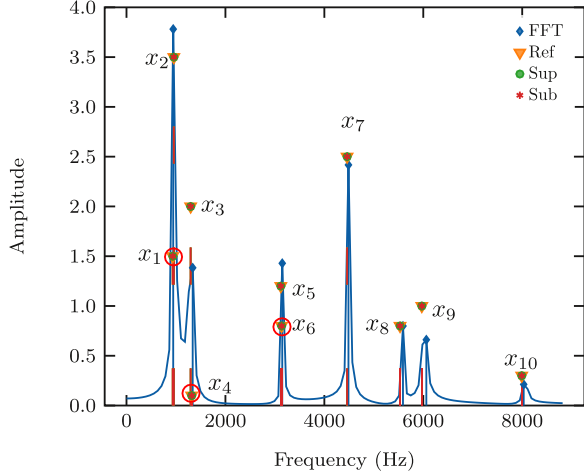


**Fig. 4** Comparison of GEM and FFT extraction accuracies of multi-frequency complex signal at different sampling frequencies, where Ref, FFT, Sup, and Sub correspond to the theoretical values of the signal components, the FFT extracted values, and the extracted values of the GEM method under Nyquist and truly sub-Nyquist sampling conditions, respectively. Additionally,  $x_1 - x_{10}$  corresponds to different components, and the components marked by the red circle indicate those that are still indistinguishable by FFT under the long-sample condition.

Despite using a sampling length that is approximately 50 times longer than that of the GEM, the FFT algorithm often struggles with smaller signal components  $x_1, x_4, x_6$ , as indicated by the red circles shown in Fig. 4. This difficulty originates from the spectral leakage and picket-fence effect inherent in FFT. These smaller components are typically obscured by the sidebands of larger-amplitude components, as precisely reflected in Table II. Such problems, common with FFT, are effectively mitigated using the GEM approach.

### B. Application Simulation

#### 1) Application of GEM Method in Ultra-Wideband Spectrum Sensing

To validate the performance of the proposed algorithm in super-resolution extraction of ultra-wideband signals, we compared the accuracy of frequency, amplitude, and phase extraction using the GEM with CSS and SFT. In the experiment, the amplitude and phase parameters of the signal are consistent with those listed in Table I. The frequency component was amplified to  $1e5$  times its original value, with the highest frequency component being approximately 0.8 GHz. The original signal sample length  $L$  for CSS and SFT ranged from 2048 to 16384, with a step size of 1024 and a sampling frequency of 2.1 times the highest component frequency. To ensure perfect reconstruction by CSS, both the

compression ratio and measurement length must satisfy the principles of perfect reconstruction [39]. The bucket parameter  $B$  of SFT must be an integer approximately equal to  $\sqrt{KL}$  [40]. The length of the filtered signal was  $6B$ , and the final compressed sample length was the maximum of CSS and SFT. For GEM, the sampling rate was 0.001 times the Nyquist sampling frequency, with sample lengths ranging from 76 to 608 points, a step size of 38, and 2000 simulations [41]. The simulation results are depicted in Fig. 5 below.

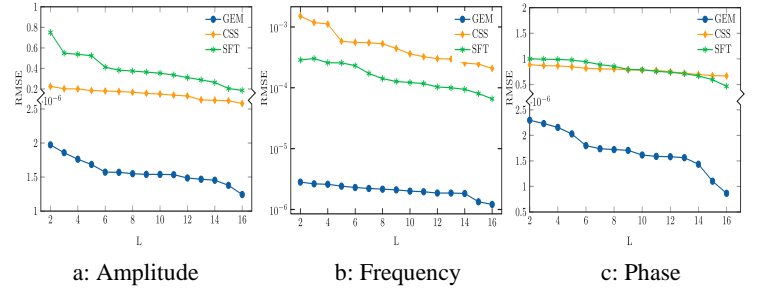


**Fig. 5** Comparison of signal parameter extraction accuracy, where GEM, CSS, and SFT correspond to the algorithm proposed in this paper, the compressed spectrum sensing algorithm, and the sparse Fourier, respectively. The figure shows the difference in the extraction accuracy of the amplitude, frequency, and phase of the signal components at different lengths.

The sub-figures (a), (b), and (c) in Fig. 5 compare the accuracy of amplitude, frequency, and phase extraction by GEM, CSS, and SFT, respectively. The horizontal axis represents the relative sample length used in the experiment, and the vertical axis represents the logarithm of the RMSE of the parameter extraction. Moreover, owing to the superior performance of GEM in amplitude and phase extraction compared to the comparative methods, a discontinuous coordinate axis method was used to display the results for these parameters.

Fig. 5 illustrates that for CSS and SFT, increasing the original sample length noticeably improves their frequency extraction accuracy, achieving approximately one order of magnitude improvement under the experimental conditions. In contrast, enhancements in amplitude and phase extraction precision were minimal. However, the proposed algorithm achieves higher accuracy in frequency, amplitude, and phase extraction with significantly lower sampling requirements—approximately 0.17 times the average length and 0.04 times the original signal length—thus outperforming standard CSS and SFT methods.

Note that while GEM can theoretically achieve accurate parameter extraction at very low sub-Nyquist sampling frequencies, it often requires increasing the duration of the signal. In practical applications such as digital transmission or GNSS positioning, each signal frame has a limited length.

> REPLACE THIS LINE WITH YOUR MANUSCRIPT ID NUMBER (DOUBLE-CLICK HERE TO EDIT) <

Therefore, the sampling time cannot exceed the frame length, imposing constraints on how low the subsampling frequency can practically be set, which is not infinitely small [42]-[44].

## 2) Application of GEM in Motion Information Extraction of Hypersonic Vehicles

presents the simulation results. As illustrated in the table, the extraction accuracy of GEM is more closely aligned with the theoretical value than that of the Wigner–Hough transform (WHT). Additionally, its error limit is nearly equivalent to the numerical accuracy. This is because the WHT method

TABLE III  
DOPPLER SHIFT EXTRACTION OF GNSS SIGNALS FOR HIGH-SPEED MOVING TARGETS BASED ON GEM AND WHT

$\theta_i$ (°)	Velocity(m/s)					Acceleration(m/s <sup>2</sup> )				
	Ref	GEM	Error of GEM	WHT	Error of WHT	Ref	GEM	Error of GEM	WHT	Error of WHT
0	680.58	680.58	1.09E-11	718.9400	5.64E-3	196.133	196.133	4.26E-09	197.2385	3.71E-4
110	-232.77	-232.7720	8.59E-12	-224.8931	3.34E-3	-67.0814	-67.0814	8.17E-10	-66.8544	1.10E-3
230	-670.24	-670.24046	9.28E-12	-721.4227	7.64E-3	-193.153	-193.153	5.26E-10	-194.6280	4.00E-3
320	118.181	118.181477	1.11E-11	131.5052	1.13E-2	34.05814	34.05814	6.35E-09	34.4421	8.55E-5

Global navigation satellite system (GNSS) receivers are widely deployed in both civilian and military domains, particularly in high-dynamic applications such as precision guidance. There exists a growing need for GNSS receivers to exhibit high reliability in highly dynamic environments. An essential aspect of capturing high-dynamic GNSS data involves accurately extracting the Doppler shift and its rate of change in the carrier signals. Owing to the characteristics of signals during rapid movements and changes, it is feasible to simplify these signals into a linear frequency-modulation (LFM) signal model during the data capture process [45], [46].

Accurately extracting the Doppler frequency and its rate of change from GNSS signals of high-speed moving targets not only corrects the frequency bias of GNSS positioning signals but also enables precise real-time inference of target motion states. Currently, velocity measurement methods based on GNSS Doppler shift are primarily categorized into two categories: derived and raw Doppler shift methods. The derived Doppler shift method offers higher accuracy in measuring the velocity of static targets, while the raw Doppler shift method excels in accuracy for targets that undergo non-uniform motion. This study focuses on utilizing the raw Doppler shift method [47], [48].

The simulation parameters are set as follows: The GNSS carrier frequency is 1.5 GHz, the initial velocity is 2 Mach, the acceleration is 20 g, with two sampling times of 500  $\mu$ s each, totaling approximately 1 ms, which corresponds to the length of a single GNSS signal. This configuration effectively avoids errors caused by phase jumps in the clock [49]. Given that the distance between the aircraft and the satellite typically exceeds 20,000 km—significantly greater than the flight distance of the aircraft during the sampling interval, as illustrated in Fig. 6—the motion speed can be projected onto the line that connects the aircraft and the satellite at an angle  $\theta_i$ . Table III

employs the FFT transform in the time-frequency transformation, and its accuracy is also influenced by factors such as spectral leakage and the pickle fence effect.

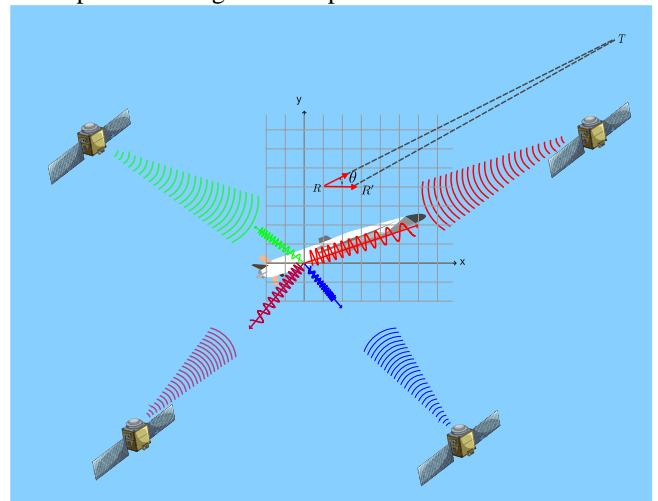


**Fig. 6** Doppler frequency offset parameter extraction for high-speed aircraft based on GEM, The figure shows the nonlinear Doppler shift of electromagnetic waves emitted by satellites located in different directions of the hypervelocity vehicle, which contains a wealth of information, including the velocity and acceleration of the vehicle.

## IV. DISCUSSION

This paper proposed a novel generalized eigenvalue signal processing algorithm that enables super-resolution at extremely low sampling frequencies. Furthermore, we applied the theory of multi-parameter eigenvalues for the first time to accurately extract the parameters of LFM signals, providing rigorous theoretical proof of its viability. The subsequent

> REPLACE THIS LINE WITH YOUR MANUSCRIPT ID NUMBER (DOUBLE-CLICK HERE TO EDIT) <

discussion revolves around comparing algorithm performance, analyzing suitable applications, and examining hardware compatibility.

#### *A. Mechanisms for Achieving Super-Resolution with GEM Truly Sub-Nyquist Sampling*

Compared with CSS and SFT, the mechanism by which the GEM achieves super-resolution under truly sub-Nyquist sampling can be explained from different perspectives using theoretical frameworks based on generalized eigenvalue theory and compressed sensing, respectively, as follows.

Within the framework of generalized eigenvalue theory, the principle of the GEM is displayed in Fig. 1: it leverages the non-coherence between rank-one matrices formed by multi-frequency signal components and their differentiated signals. By employing a synchronous aliasing mechanism, it effectively avoids the SL and picket-fence effect inherent in DFT, thus offering higher precision in super-resolution extraction. Moreover, GEM utilizes the density or infinite divisibility of its eigenvalues in the numerical domain to effectively circumvent the frequency collision problem present in the standard SFT.

Under the framework of compressed sensing, the principle of GEM operates as follows: The infinite sparse representation vectors of the original signal and its differentiated signal within the generalized multi-frequency framework maintain consistent non-zero element positions, changing only in their sparse coefficients. When solving for these coefficients, GEM does not directly determine the precise sparse coefficients of the original and differentiated signals. Instead, it computes the ratios of the sparse coefficients that share the same non-zero element positions, which correspond to the precise frequency values of the signal components. This method avoids problems such as destroyed sparsity due to SL and the picket-fence effect, which commonly affect other compressed sensing spectrum methods, thereby ensuring exact extraction of signal components.

It is crucial to emphasize that the necessary length of the measurement data for the GEM method is entirely determined by the number of signal components, reflecting the inherent sparsity of the signal. This characteristic enables GEM to accurately extract the parameters of signal components even with limited sample sizes, demonstrating its potential advantages in the realm of CSS.

In practical applications such as cognitive radio systems and UWB communication, the GEM method offers significant advantages. It is especially well-suited for situations where the signal bandwidth is wide, standard sampling rates fail to satisfy the Nyquist criteria, and data collection time is limited. In many cases, signal frequencies are densely packed and dynamically changing, posing challenges for conventional methods that rely on extensive prior information. The GEM method excels by exactly extracting signal amplitudes and phases without heavy reliance on prior data. It efficiently retrieves multi-frequency signal components with high resolution from short data segments across varying sampling frequencies.

#### *B. Hardware Compatibility*

Compared to other random sampling methods in CSS, the proposed algorithm utilizes uniform sampling for truly sub-Nyquist sampling. This approach facilitates a more practical and cost-effective hardware implementation solution. The required components include commercial-grade low-pass filters, first-order derivative samplers, standard low-rate sampling components, analog-to-digital converters (ADCs), and digital signal processors (DSPs). The implementation simplifies hardware design, reduces costs, and is straightforward to integrate into existing signal processing systems. It opens up new opportunities for the practical application and commercialization of compressed sensing technology.

#### *C. Issues and Concerns*

Importantly, although the GEM method provides a very low sampling rate, this is achieved at the expense of a longer sampling time. In certain applications, such as digital wireless communications, this may cause the sampling time to exceed the length of the unit data frame, which may result in skipping transitions and therefore should be avoided. Additionally, compared to traditional DFT-based CSS, our proposed method may have some limitations in terms of signal types that can be applied to continuous band signals. This will be one of the topics of our further research.

## V. CONCLUSION

This study proposed an innovative signal processing technique called the GEM, which operates at sub-Nyquist sampling frequencies 0.001 times the signal bandwidth and uses only 10% of the sampling length required by other compressed spectral sensing methods. GEM greatly improves reconstruction precision by approximately three to four orders of magnitude. The algorithm successfully achieved super-resolution reconstruction of multi-frequency complex signals at ultra-low sampling rates, and we fully validated its theoretical rationale. Furthermore, the GEM has been extended to extract characteristic parameters from LFM signals. From a hardware perspective, the proposed algorithm can be easily implemented using existing commercial devices without requiring new hardware development, thus significantly simplifying hardware design auto-comp and reducing costs. This opens up new opportunities for practical and commercial applications of compressed sensing technology.

Notably, while the GEM shows clear advantages over Fourier-based CSS algorithms in accurately estimating characteristic parameters under sub-Nyquist sampling for standard sparse signals, and has successfully achieved precise extraction of LFM signals, its applicability across various signal types requires further research compared to Fourier-based methods. Moreover, the robustness of the proposed algorithm under noisy conditions needs to be thoroughly assessed, which is crucial for ensuring its reliability in practical applications.

## REFERENCES

- [1] J. Yhang *et al.*, "5G millimeter-wave antenna array: Design and challenges," *IEEE Wireless Commun.*, vol. 24, no. 2, pp. 106-112, Apr. 2016.
- [2] J. D. Taylor, *Ultra-Wideband Radar Systems*. Boca Raton, FL, USA: CRC Press, 2001.
- [3] J. Tian and K.-K. Ma, "A survey on super-resolution imaging," *Signal Image Video Process.*, vol. 5, no. 3, pp. 329-342, Sep. 2011.
- [4] M. Mishali and Y. C. Eldar, "From Theory to Practice: Sub-Nyquist Sampling of Sparse Wideband Analog Signals," *IEEE J. Sel. Topics Signal Process.*, vol. 4, no. 2, pp. 375-391, Apr. 2010.
- [5] Y. C. Eldar, P. Kuppinger, and H. Bolcskei, "Compressed Sensing for Analog Signals in Shift-Invariant Spaces," *IEEE Trans. Signal Process.*, vol. 58, no. 5, pp. 2626-2637, May 2010.
- [6] M. Mishali, A. Elron, and Y. C. Eldar, "Sub-Nyquist processing with the modulated wideband converter," in *Proc. IEEE Int. Conf. Acoust. Speech Signal Process.*, Dallas, TX, USA, 2010, pp. 3898-3901.
- [7] E. Israeli *et al.*, "Hardware calibration of the modulated wideband converter," in *Proc. IEEE Global Commun. Conf.*, Austin, TX, USA, 2014, pp. 948-953.
- [8] M. Mishali and Y. C. Eldar, "From Theory to Practice: Sub-Nyquist Sampling of Sparse Wideband Analog Signals," *IEEE J. Sel. Topics Signal Process.*, vol. 4, no. 2, pp. 375-391, Apr. 2010.
- [9] Y. C. Eldar and T. Michaeli, "Xampling: Analog to Digital at Sub-Nyquist Rates," *IEEE Trans. Inf. Theory*, vol. 60, no. 7, pp. 4094-4110, Jul. 2014.
- [10] M. Mishali, Y. C. Eldar, O. Dounaevsky, and E. Shoshan, "Xampling: Compressed Sampling for Analog Signals," *IEEE Signal Process. Mag.*, vol. 28, no. 3, pp. 88-102, May 2011.
- [11] M. Mishali, Y. C. Eldar, and A. J. Elron, "Xampling: Signal acquisition and processing in union of subspaces," *IEEE Trans. Signal Process.*, vol. 59, no. 10, pp. 4719-4734, Oct. 2011.
- [12] M. Kapralov, "Sparse Fourier transform in any constant dimension with nearly-optimal sample complexity in sublinear time," in *Proc. 48th Annu. ACM Symp. Theory Comput.*, Cambridge, MA, USA, 2016, pp. 264-277.
- [13] H. Hassanieh *et al.*, "Nearly optimal sparse Fourier transform," in *Proc. 44th Annu. ACM Symp. Theory Comput.*, New York, NY, USA, 2012, pp. 563-578.
- [14] P. Indyk, M. Kapralov, and E. Price, "(Nearly) sample-optimal sparse Fourier transform," in *Proc. 25th Annu. ACM-SIAM Symp. Discrete Algorithms*, Portland, OR, USA, 2014, pp. 480-499.
- [15] D. Romero and G. Leus, "Compressive covariance sampling," in *Proc. Inf. Theory Appl. Workshop*, San Diego, CA, USA, 2013, pp. 1-8.
- [16] D. Romero *et al.*, "Compressive Covariance Sensing: Structure-based compressive sensing beyond sparsity," *IEEE Signal Process. Mag.*, vol. 33, no. 1, pp. 78-93, Jan. 2016.
- [17] H. Rauhut, "Compressive sensing and structured random matrices," *Theor. Found. Numer. Methods Sparse Recovery*, vol. 9, no. 1, pp. 92-133, 2010.
- [18] F. Krahmer and H. Rauhut, "Structured random measurements in signal processing," *GAMM - Mitteilungen*, vol. 37, no. 2, pp. 217-238, 2014.
- [19] M. C. Angelini, F. Ricci-Tersenghi, and Y. Kabashima, "Compressed sensing with sparse, structured matrices," in *Proc. 50th Annu. Allerton Conf. Commun. Control Comput.*, Monticello, IL, USA, 2012, pp. 808-814.
- [20] T. T. Do, T. D. Tran, and L. Gan, "Fast compressive sampling with structurally random matrices," in *Proc. IEEE Int. Conf. Acoust. Speech Signal Process.*, Las Vegas, NV, USA, 2008, pp. 3369-3372.
- [21] J. N. Laska *et al.*, "Theory and Implementation of an Analog-to-Information Converter using Random Demodulation," in *Proc. IEEE Int. Symp. Circuits Syst.*, New Orleans, LA, USA, 2007, pp. 1959-1962.
- [22] S. Pfetsch *et al.*, "On the feasibility of hardware implementation of sub-Nyquist random-sampling based analog-to-information conversion," in *Proc. IEEE Int. Symp. Circuits Syst.*, Seattle, WA, USA, 2008, pp. 1480-1483.
- [23] M. F. Duarte and R. G. Baraniuk, "Spectral compressive sensing," *Appl. Comput. Harmon. Anal.*, vol. 35, no. 1, pp. 111-129, Jul. 2013.
- [24] R. G. Baraniuk *et al.*, "Model-based compressive sensing," *IEEE Trans. Inf. Theory*, vol. 56, no. 4, pp. 1982-2001, Apr. 2010.
- [25] L. Xiao and X.-G. Xia, "Frequency determination from truly sub-Nyquist samplers based on robust Chinese remainder theorem," *Signal Process.*, vol. 150, pp. 248-258, Sep. 2018.
- [26] D. L. Donoho, A. Maleki, and A. Montanari, "The noise-sensitivity phase transition in compressed sensing," *IEEE Trans. Inf. Theory*, vol. 57, no. 10, pp. 6920-6941, Oct. 2011.
- [27] Y. H. Gu and M. H. J. Bollen, "Estimating interharmonics by using sliding-window ESPRIT," *IEEE Trans. Power Del.*, vol. 23, no. 1, pp. 13-23, Jan. 2008.
- [28] V. Dumoulin *et al.*, "On the challenges of physical implementations of RBMs," in *Proc. AAAI Conf. Artif. Intell.*, Quebec City, QC, Canada, 2014, pp. 2304-2310.
- [29] M. Fardad, S. M. Sayedi, and E. Yadyan, "Hardware implementation of iterative method with adaptive thresholding for random sampling recovery of sparse signals," *IEEE Trans. Very Large Scale Integr. (VLSI) Syst.*, vol. 26, no. 5, pp. 867-877, May 2018.
- [30] W. Shi *et al.*, "Image compressed sensing using convolutional neural network," *IEEE Trans. Image Process.*, vol. 29, pp. 375-388, 2020.
- [31] D. L. Boley, F. T. Luk, and D. Vandevoorde, "Vandermonde factorization of a Hankel matrix," *Sci. Comput.*, pp. 27-39, 1997.
- [32] D. L. Boley, F. T. Luk, and D. Vandevoorde, "A fast method to diagonalize a Hankel matrix," *Linear Algebra Appl.*, vol. 284, no. 1-3, pp. 41-52, Nov. 1998.
- [33] J. S. Vandergraft, "Generalized Rayleigh methods with applications to finding eigenvalues of large matrices," NASA, Washington, D.C., USA, Tech. Rep. NASA-CR-110448, 1970.
- [34] J. Gilbert and L. Gilbert, *Linear Algebra and Matrix Theory*. Amsterdam, Netherlands: Elsevier, 2014.
- [35] M. E. Hochstenbach, C. Mehl, and B. Plestenjak, "Solving singular Generalized eigenvalue problems by a rank-completing perturbation," *SIAM J. Matrix Anal. Appl.*, vol. 40, no. 3, pp. 1022-1046, 2019.
- [36] Muhić and B. Plestenjak, "On the singular two-parameter eigenvalue problem," *Electron. J. Linear Algebra*, vol. 18, pp. 420-437, 2009.
- [37] G. Hori, "Comparison of two main approaches to joint SVD," in *Proc. Int. Conf. Indep. Compon. Anal. Signal Sep.*, Paraty, Brazil, 2009, pp. 709-716.
- [38] G. Hori, "Joint SVD and its application to factorization method," in *Proc. Int. Conf. Latent Variable Anal. Signal Sep.*, St. Malo, France, 2010, pp. 172-179.
- [39] D. L. Donoho, "Compressed Sensing," *IEEE Trans. Inf. Theory*, vol. 52, no. 4, pp. 1289-1306, Apr. 2006.
- [40] H. M. Kasem and M. El-Sabrouty, "A comparative study of audio compression based on compressed sensing and sparse fast Fourier transform (SFFT): Performance and challenges," in *Proc. IEEE Int. Symp. Signal Process. Inf. Technol.*, Athens, Greece, 2013, pp. 000219-000224.
- [41] K. Kikuta and A. Hirose, "Direction-of-arrival estimation of ultra-wideband signals in narrowband interference environment based on power inversion and complex-valued neural networks," *Neural Process. Lett.*, vol. 47, pp. 921-933, Jun. 2018.
- [42] X. Huang, X. Zhao, and W. Lu, "Joint frequency and DOA estimation of sub-Nyquist sampling multi-band sources with unfolded coprime arrays," *Multidimens. Syst. Signal Process.*, vol. 33, no. 4, pp. 1257-1272, Nov. 2022.
- [43] X. Li *et al.*, "Accuracy and reliability of multi-GNSS real-time precise positioning: GPS, GLONASS, BeiDou, and Galileo," *J. Geodesy*, vol. 89, no. 6, pp. 607-635, Jun. 2015.
- [44] J. Terry and J. Heiskala, *OFDM Wireless LANs: A Theoretical and Practical Guide*. Indianapolis, IN, USA: Sams Publishing, 2002.
- [45] F. Gao and H. Xia, "Fast GNSS signal acquisition with Doppler frequency estimation algorithm," *GPS Solut.*, vol. 22, no. 1, pp. 1-13, Jan. 2018.
- [46] S.-H. Kong, "High sensitivity and fast acquisition signal processing techniques for GNSS receivers: From fundamentals to state-of-the-art GNSS acquisition technologies," *IEEE Signal Process. Mag.*, vol. 34, no. 5, pp. 59-71, Sep. 2017.
- [47] F. Guo *et al.*, "Instantaneous velocity determination and positioning using Doppler shift from a LEO constellation," *Satell. Navig.*, vol. 4, no. 1, pp. 1-9, Feb. 2023.
- [48] Angrisano *et al.*, "Velocity Estimation Using Time-Differenced Carrier Phase and Doppler Shift with Different Grades of Devices: From Smartphones to Professional Receivers," *Algorithms*, vol. 17, no. 1, pp. 1-16, Jan. 2023.
- [49] J. Öström *et al.*, "Effects of datalink target data on air-to-air missile performance," *J. Def. Model. Simul.*, vol. 21, no. 3, pp. 323-340, 2024.

> REPLACE THIS LINE WITH YOUR MANUSCRIPT ID NUMBER (DOUBLE-CLICK HERE TO EDIT) <



**Baoguo Liu** received the B.S. degree in grain machinery from Zhengzhou Grain University, Zhengzhou, China, in 1982, the M.S. degree in solid mechanics from the Dalian University of Technology, Dalian, China, in 1986, and the Ph.D. degree in solid mechanic from Chongqing University, Chongqing, China, in 2002.

Since 2004, he has been a Professor with the Henan University of Technology. He has authored three books and more than 50 articles. His research interests include signal processing, fault diagnosis and motor dynamics. He has presided four NSFC projects and more than ten other scientific research projects. He was China's National 863 Project, the National Natural Science Foundation of China, China's National Youth Thousand Assessment Experts.



**Huiguang Zhang** graduated from Southwest Jiaotong University (SWJTU) in 2007 with a Bachelor's degree in Engineering and graduated from SWJTU in 2010 with a Master's degree. He is currently pursuing his Ph.D. degree at Henan University of Technology. His research interests include signal processing.



**Wei Feng** received the B.S. degree in mechanical engineering and automation from the Wuhan University of Technology, Wuhan, China, in 2004, the M.S. degree in mechanical engineering from Xi'an Jiaotong University, Xian, China, in 2011, the Ph.D. degree in machine building and automation from

Xiamen University, Xiamen, China, in 2016. Since 2016, he has been an Assistant Professor of mechanical engineering with the Henan University of Technology. He is the author of 25 articles. His research interests include signal processing and mechanical dynamics.